2024 IEEE/RSJ International Conference on Intelligent Robots and Systems (IROS)
October 14-18, 2024. Abu Dhabi, UAE

A Geometry-based Approach for Support-free Additive Manufacturing of Structures with Large Overhang Angles and Closed Features

Jitian Liu[1], Zachary Cohen[2], Jin Seob Kim[1], Mehran Armand[3], and Michael D. M. Kutzer[2]

***Abstract*— Architected materials derive performance characteristics from material properties and internal geometry. These materials are increasingly prevalent across a wide variety of domains. Many intricate feature geometries associated with architected materials can be explored using additive manufacturing (AM) processes. However, current AM methods generally cannot fabricate geometries with completely closed voids without introducing a support structure. This paper describes a new, support-free approach to AM capable of creating structures with closed voids. This work limits part geometry to three-dimensional (3D) geometries defined by a revolution about a single axis. This limitation enables planar analysis within a three-degree-of-freedom (3-DoF) task space. Part geometry in 3-DoF task space is constrained to a convex arch. Task space geometry is divided into an ordered set of sub-regions, considering feasible deposition orientations and collision constraints. The use of 3-DoF task space provides planar translation and rotation of the component during fabrication. The introduction of this rotational DoF addresses AM overhang constraints imposed by gravity. Methods for generating, ordering, and layering sub-regions suitable for printing a part with a closed hole are presented. Layers derived in the 3-DoF task space analysis are then extended to 3D deposition paths using the axis of revolution defined by the original part. The method of hole closure relies on the concept of a "keystone" which requires a 45° nozzle offset for collision-free deposition within keystone-adjacent sub-regions. The feasibility of deposition using a 45° nozzle offset is explored experimentally, and results demonstrate feasibility.**

I. Introduction

Architected materials are used across a range of medical, scientific, commercial, defense, and engineering applications. These materials rely on complex, three-dimensional (3D) geometric features to tailor properties for specific applications. 3D features can range from the macroscale to the nanoscale to obtain desired characteristics. Examples of architected materials include lattice structures to increase strength, toughness, and/or stiffness-to-weight ratios [1], [2], load-bearing structures with radar absorption characteristics [3], and surface finishes to improve biocompatibility of implants [4].

The realization of these tuned material properties is limited by existing design, modeling, and fabrication capabilities [5]. Unlike parts fabricated using traditional methods, architected materials rely on complex internal and/or external geometries to achieve specific design goals. Many of these designs contain large numbers of deliberate, recurring voids creating branched and/or interlaced features on a scale smaller than the overall functional part [2]. Additive manufacturing (AM) technology has expanded the exploration and utilization of architected materials on various scales despite limitations [2]. Notably, architected materials designed for fabrication using AM processes are typically constrained to contain open voids [6]. Closed voids are commonly used in extrusion-based AM fabrication (e.g., fused filament fabrication) in the form of "infill geometry." Adaptation of existing infill geometries has been explored to enhance material properties [7], and work continues to develop novel infill geometries (e.g. [8]) and infill permitting continuous deposition paths [9], [10]. These efforts show the feasibility of AM of closed-cell architected materials with infill geometry limited by the AM process overhang constraints realized in a Cartesian stage AM process. This work presents a method to expand the viable set of closed-cell geometries that can be fabricated using AM.

Beyond AM, numerous alternate methods exist to create architected materials leveraging closed-cell structures. These commonly leverage a multistep fabrication process with examples including honeycomb lattices with applied face sheets [11] and structural closed-cell foams [12]. While effective for large-scale production of architected materials, these methods are limited to a subset of void geometries that are typically homogeneous. AM can address this limitation, providing a critical capability in fabricating highly tunable, non-uniform closed-cell structures.

AM capabilities have been expanded using robotics technology [13]. Robotic manipulation extends the space of realizable AM geometries by increasing articulation between the deposition head and the build surface. This has enabled methods for creating support-free thin shell parts [14], conformal AM parts [15], and support-free AM parts [16]–[18] have been demonstrated. The drawback to the additional articulation of these systems is an increase in planning complexity. Specifically, realizing a deposition path along a non-flat surface using a high-DoF system (e.g., a serial manipula-

*This work was supported by the Office of Naval Research FY22 Grant No. N0001422WX01976 and FY23 Grant No. N0001423WX02035.

[1]These authors are with the Department of Mechanical Engineering, Johns Hopkins University, Baltimore, Maryland 21218, USA (emails: jliu309@jhu.edu, jkim115@jhu.edu)

[2]These authors are with the Department of Weapons, Robotics, & Control Engineering, United States Naval Academy, Annapolis, Maryland 21402, USA (emails: kutzer@usna.edu, zcohen@usna.edu)

[3]This author is with the Departments of Orthopaedic Surgery, Mechanical Engineering, & Computer Science, Johns Hopkins University, Baltimore, Maryland 21218, USA (email: marmand2@jhu.edu)

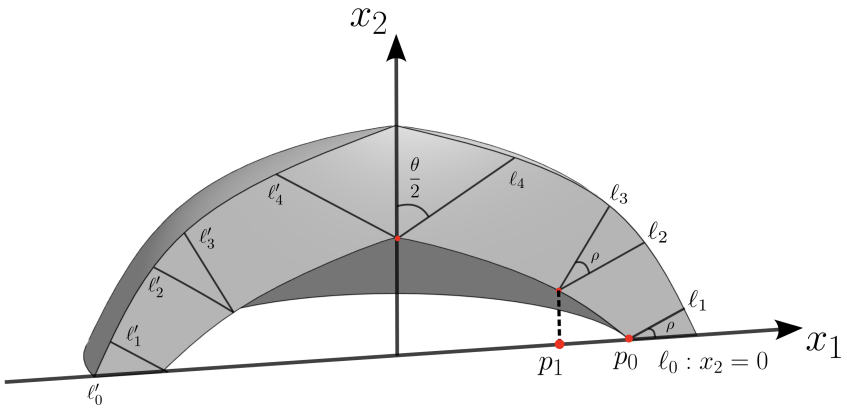

Fig. 1. A printable partition of a convex arch, which is shown as a cross-section of a convex dome. Note that $n = 1$ in this example.

tor) presents numerous collision opportunities. Research into collision-free planning for these systems has demonstrated the feasibility of deposition onto constrained sets of locally concave surfaces [19], and methods to decompose parts into discrete, connected sub-volumes that can be manufactured using traditional planning [16]–[18], [20]. These methods establish a support-free approach to AM of complex, open structures but do not address AM of closed voids. A recent analysis of AM in a 2D workspace has proposed a method to address this limitation by introducing concepts of non-normal deposition and "keystone shapes" (which pertain to parts that are fabricated by depositing material into a wedge- or cone-shaped concavity) [21].

This paper, as an extension of [21], explores the feasibility of support-free AM in the context of 3D part geometries containing closed voids. Part geometry and voids are constrained to geometries defined about a single axis of revolution. This initial study assumes an extrusion-based AM method with constraints similar to fused filament fabrication (FFF). Inspired by [16]–[18], [20], this work leverages a decomposition approach to account for constraints associated with material overhang and nozzle/part collisions. In this work, revolved geometry is limited to a convex half-ring. For brevity, only the top half of the half-ring (the *convex dome*) is explored, noting that support-free AM of the bottom-half region (the *convex bowl*) can be fabricated using methods described in [16]–[18].

Section II formulates (a) the problem to be addressed in this paper (i.e., printing a dome-shaped structure), (b) strictly defines a convex dome and a convex arch, which characterizes the target geometry to be printed, and (c) defines overhang and collision constraints in the process of 3D printing. Section III addresses the problem of printing a convex arch in a 2D workspace, whereas Section IV serves as an extension of the contents in Section III to a 3D workspace. Section V describes the feasibility testing conducted to evaluate the feasibility of FFF using a 45° nozzle angle relative to the deposition direction, and Section VI summarizes the experimental test results. Results show successful FFF using a 45° nozzle angle. These results demonstrate the feasibility of non-normal AM in the context of FFF and suggest the future viability of the methods presented.

II. Definitions and Overview of the Problem

This paper aims to print a *convex dome* structure in the bottom-up order by switching between a finite number of printer nozzles. This section aims to strictly define convex domes, *convex arches*, as well as the *overhang and collision constraints* in 3D printing. These definitions will be used throughout the paper.

Definition 1. *Let $0 < R_1 < R_2$. Consider two continuous, concave, and monotonically decreasing functions $f_1 : [0, R_1] \to \mathbb{R}_{\geq 0}$ and $f_2 : [0, R_2] \to \mathbb{R}_{\geq 0}$. Suppose that $f_1(\sigma) < f_2(\sigma)$ for any $\sigma \in [0, R_1]$. Let $\mathcal{D}_1$ and $\mathcal{D}_2$ be two compact subsets of $\mathbb{R}^2$ with*

$$\begin{aligned}&\mathcal{D}_1(f_1, f_2) = \\ &\{x \in [0, R_1] \times \mathbb{R}^2 : f_1(x_1)^2 \leq x_2^2 + x_3^2 \leq f_2(x_1)^2\}\end{aligned} \tag{1}$$

and

$$\mathcal{D}_2(f_2) = \{x \in [R_1, R_2] \times \mathbb{R}^2 : x_2^2 + x_3^2 \leq f_2(x_1)^2\}. \tag{2}$$

*Then the **convex dome** defined by f_1 and f_2 is the set $\mathcal{D}(f_1, f_2) = \mathcal{D}_1(f_1, f_2) \cup \mathcal{D}_2(f_2)$.*

Intuitively, a convex dome is a body of revolution whose radial cross-section is a "strip" bounded by f_1 and f_2. Below is the formal definition of the "strip":

Definition 2. *Take the notations used in Definition 1. Let*

- *$\mathcal{D}(f_1, f_2)$ be a convex dome defined above,*
- *$u \in \{x \in \mathbb{R}^3 : x_1 = 0\}$ be a vector, and*
- *$u^\perp = \{v \in \mathbb{R}^3 : v^\top u = 0\}$.*

*Then the set $\mathcal{S} \coloneqq u^\perp \cap \mathcal{D}(f_1, f_2)$ is called a **convex arch**.*

The nozzle geometry will be considered as a compact subset of $\mathbb{R}^n$ ($n = 2, 3$). The overhang and collision constraints are defined as follows:

Definition 3. *Let $\Gamma, \mathcal{N} : [0, \infty) \to \mathbb{R}^n$ ($n = 2, 3$) respectively denote the geometry that is fabricated and the nozzle geometry. The **collision constraint** is satisfied if*

$$\mu(\mathcal{N}(t) \cap \Gamma(t)) = 0, \quad \forall\, t \geq 0, \tag{3}$$

*and violated otherwise. Here $\mu(E)$ denotes the Lebesgue measure of a set $E \subset \mathbb{R}^n$. Let $K(t, T)$ be the affine space that will be taken as the printing bed during time $[t, t + T]$ and $\Gamma_{t,T} = \Gamma(t + T) \setminus \Gamma(t)$. The **overhang constraint** is satisfied if, for any $p \in \partial\Gamma_{t,T}$ at which $\partial\Gamma_{t,T}$ is smooth,*

$$\angle(T_p^a \partial\Gamma_{t,T}, K(t, T)) < \frac{\pi}{2} + \gamma, \tag{4}$$

*where $T_p^a\mathcal{M}$ represents the affine space that is tangent to $\mathcal{M}$ at $p \in \mathcal{M}$, and $\angle(L_1, L_2)$ denotes the angle between two affine spaces L_1 and L_2. $\gamma < \pi/2$ is called the **overhang constraint angle**.*

Note that, according to Definition 3, contacts between the nozzle and fabricated part(s) at their vertices, edges, or faces (if in 3D) will not be considered a violation of the collision constraint. Also, one should not expect that $\mathcal{N}(t_1)$ and $\mathcal{N}(t_2)$ are congruent for any $t_1 \neq t_2$, since, as stated at the beginning of this section, different nozzles may be used in the process of printing. Another important assumption is that, in this paper, *the nozzle is allowed to deposit material without being normal to its deposition trajectory.* In the next two sections, the printability of convex arches and convex domes will be investigated, along with constructive proofs to demonstrate the feasibility of fabricating them.

III. Printability of a Convex Arch in a 2D Workspace

Consider a 2D nozzle that can be freely re-oriented in $\mathbb{R}^2$. It is desired that, given a convex arch, a partition is computed such that the nozzle(s) may traverse a collision-free path without violating the overhang constraints when printing each shape in the partition in a bottom-up order. In particular, one may claim the following:

Proposition 1. *Let $\mathcal{D}(f_1, f_2)$ be a convex dome and $\mathcal{S}$ its convex arch. Then there exists a printable partition of $\mathcal{S}$.*

Proof: For conformation to the convention that the x_2-axis is taken as the vertical axis, flip $\mathcal{S}$ about the line $x_2 = x_1$ such that its base aligns to the x_1-axis. Notice that this action is equivalent to swapping the x_1 and x_2 axes such that the boundaries of $\mathcal{S}$ are defined by f_1^{-1} and f_2^{-1} (recall that, for a bijective function $f : \mathbb{R} \to \mathbb{R}$, the graphs of f and f^{-1} are symmetric about the line $x_2 = x_1$). Let γ be the overhang constraint angle. Assume without loss of generality that

1) f_1 and f_2 are bijective,
2) $f_1(R_1) = 0$, and
3) $\theta_0 = \tan^{-1}(\partial_{x_1} f_1^{-1}(f_1(0)^-)) > \pi/2 + \gamma$, where $\partial_{x_1} f(x^-)$ means the left derivative of f w.r.t. x_1 at $x_1 = x$. Throughout the proof, the co-domain of $\tan^{-1}(\cdot)$ is $[0, \pi) \setminus \{\pi/2\}$.

(i.e., the dome has a non-flat ceiling, and the inclination angle at its base exceeds the overhang constraint). If $\theta_0 \leq \pi/2 + \gamma$, then one may adopt traditional horizontal layering until the overhang constraint is violated. Otherwise, one may generate a printable partition of $\mathcal{S}$ via the following procedure:

1) Choose some $\rho < \pi/2$ such that $\theta_0 - \rho < \gamma + \pi/2$.
2) Let $p_0 = f_1(0)$. Find $p_1, ..., p_n \in [0, f_1(0))$ such that
   - $p_0 > p_1 > \cdots > p_n > 0$,
   - for any $1 \leq k \leq n$,
   $$\pi > \tan^{-1}[\partial_{x_1} f_1^{-1}(p_k^-)] = \frac{\pi}{2} + \gamma + k\rho, \tag{5}$$
   - for any $p \in [0, p_n)$,
   $$\tan^{-1}[\partial_{x_1} f_1^{-1}(p^-)] \leq \frac{\pi}{2} + \gamma + (n+1)\rho \leq \pi \tag{6}$$

   Intuitively, $\{p_i\}_{i \geq 1}$ are the points at which the printing bed needs to be reoriented. The criteria above also indicate that n will not be infinitely large. Rather, from (6) one has that
   $$n \leq \frac{1}{\rho}\left(\frac{\pi}{2} - \gamma\right) - 1 \tag{7}$$
   and it is worth noting (again, from (6)) that, for any $k \in \{1, ..., n+1\}$,
   $$k\rho \leq (n+1)\rho \leq \frac{\pi}{2} - \gamma \tag{8}$$
3) Define the lines $\ell_0, \ell_1, ..., \ell_{2n+1}$ with
   $$\ell_k : x_2 = f_1^{-1}\left(p_{\frac{k-1}{2}}\right) + \tan\left[\frac{(k+1)\rho}{2}\right]\left[x_1 - p_{\frac{k-1}{2}}\right] \tag{9}$$
   if k is odd, and
   $$\ell_k : x_2 = f_1^{-1}\left(p_{\frac{k}{2}}\right) + \tan\left(\frac{k\rho}{2}\right)\left(x_1 - p_{\frac{k}{2}}\right) \tag{10}$$
   if k is even.
4) Choose some $\theta < \pi$ and define $\ell_{2n+2} : x_2 = f_1^{-1}(0) + \tan((\pi - \theta)/2)x_1$ and reflect $\ell_0, ..., \ell_{2n+2}$ about the x_2-axis to obtain $\ell_0', ..., \ell_{2n+2}'$. Then a printable partition of $\mathcal{S}$ is generated by splitting $\mathcal{S}$ with $\{\ell_i\}_{i=0}^{2n+2}$ and $\{\ell_i'\}_{i=0}^{2n+2}$.

One may refer to Fig. 1 for a visual illustration of the outcome of the procedure above. Now let S_i be the part of $\mathcal{S}$ that lies between ℓ_i and ℓ_{i-1} ($i = 1, ..., (2n+2)$), and define S_i' in a similar way. Finally, let

$$S^* = \mathcal{S} \setminus \bigcup_{i=1}^{2n+2} (S_i \cup S_i'). \tag{11}$$

It is desired to show that $\mathcal{S}$ can be printed by printing the shapes in the following order:

$$S_1 \to S_1' \to \cdots \to S_{2n+2} \to S_{2n+2}' \to S^*. \tag{12}$$

To verify that the overhang constraints will not be violated, note that, when $i \in \{1, ..., 2n+2\}$ is odd, the inclination angle α_i of S_i relative to its printing bed (i.e., ℓ_{i-1}) has that

$$\alpha_i \leq \max\Bigg\{\rho, \pi - \tan^{-1}\left[\partial_{x_1} f_2^{-1}\left(\hat{p}_i^-\right)\right] - \frac{(i-1)\rho}{2}\Bigg\}, \tag{13}$$

where $\hat{p}_i$ is the x_1 coordinate of the intersection between ℓ_i and the graph of f_2^{-1} (and this notation will be used in the rest of the proof). Note that the second term is also smaller than $\pi/2$ because $\tan^{-1}\left[\partial_{x_1} f_2^{-1}\left(\hat{p}_i^-\right)\right] > \frac{\pi}{2}$. Hence S_i and S_i' satisfy the overhang constraint when i is odd. When i is even, by construction, one has that, because $\partial_{x_1} f_j^{-1}(x^+) \leq \partial_{x_1} f_j^{-1}(x^-)$ for $j = 1, 2$ and the derivatives of f_1^{-1} and f_2^{-1} are non-increasing,

$$\begin{aligned}
\alpha_i &\leq \max\Bigg\{\tan^{-1}\left[\partial_{x_1} f_1^{-1}\left(p_{\frac{i}{2}}^+\right)\right] - \frac{i\rho}{2}, \tan^{-1}\left[\partial_{x_1} f_2^{-1}(\hat{p}_i^+)\right] - \frac{i\rho}{2}\Bigg\} \\
&\leq \max\Bigg\{\tan^{-1}\left[\partial_{x_1} f_1^{-1}\left(p_{\frac{i}{2}}^-\right)\right] - \frac{i\rho}{2}, \tan^{-1}\left[\partial_{x_1} f_2^{-1}(\hat{p}_i^-)\right] - \frac{i\rho}{2}\Bigg\} \\
&= \max\left\{\frac{\pi}{2} + \gamma,\ \tan^{-1}\left[\partial_{x_1} f_2^{-1}(\hat{p}_i^-)\right] - \frac{i\rho}{2}\right\}.
\end{aligned} \tag{14}$$

One may immediately conclude that the overhang constraints will not be violated when printing S_i and S_i', as long as

$$\frac{\pi}{2} + \gamma \geq \tan^{-1}\left[\partial_{x_1} f_2^{-1}(\hat{p}_i^-)\right] - \frac{i\rho}{2}. \tag{15}$$

Otherwise, only a subset of S_i and S_i' will be printable. To address such scenarios, one may partition S_i into two sub-shapes $S_{i,1}$ and $S_{i,2}$, where $S_{i,1}$ is the largest subset of S_i that can be fabricated within the overhang constraint and $S_{i,2} = S_i \setminus S_{i,1}$, and print $S_{i,1}$ before $S_{i,2}$, as shown in Fig. 2.

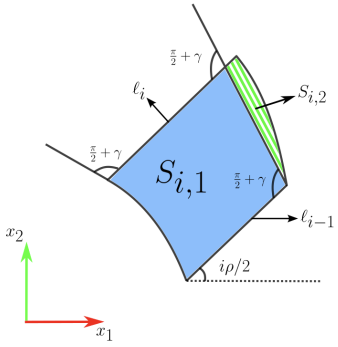

Fig. 2. A printable partition of S_i when i is even, and the shape cannot be printed in one single step. The green lines that fill $S_{i,2}$ represent the nozzle's trajectories of deposition.

Note that, by letting

$$\theta_{i,2}^* = \min_{x \in [\hat{p}_i, \hat{p}_{i-1}]} \tan^{-1}\left[\partial_{x_1} f_2^{-1}(x^-)\right] \tag{16}$$

($\theta_{i,2}^* \geq \pi/2$), the largest inclination angle relative to the printing bed when printing $S_{i,2}$ is ($x \in [\hat{p}_i, \hat{p}_{i-1}]$ below),

$$\begin{aligned}
\alpha_{i,2} &\leq \max\left\{\frac{\pi}{2} + \gamma, \pi - \left(\frac{\pi}{2} + \gamma - \frac{i\rho}{2}\right) - \tan^{-1}\left[\partial_{x_1} f_2^{-1}(x^-)\right]\right\} \\
&\leq \max\left\{\frac{\pi}{2} + \gamma, \frac{\pi}{2} - \gamma + \frac{i\rho}{2} - \theta_{i,2}^*\right\} \\
&\overset{\text{by (5)}}{\leq} \max\left\{\frac{\pi}{2} + \gamma, \pi - 2\gamma - \theta_{i,2}^*\right\} \\
&\leq \max\left\{\frac{\pi}{2} + \gamma, \frac{\pi}{2} - 2\gamma\right\} \\
&= \frac{\pi}{2} + \gamma.
\end{aligned} \tag{17}$$

Therefore $S_{i,2}$ can be printed within the overhang constraints. As for S^*, since it will be fully supported by ℓ_{2n+2} and ℓ_{2n+2}', it can be safely fabricated even when $\theta/2 > \gamma$.

To address the collision constraints, note that, upon the completion of S_i and S_i', the fabricated geometry is completely outside the wedge $\mathcal{W}_i$ that is formed by ℓ_i and ℓ_i' and opens upward (see Fig. 3). Therefore, when printing S_{i+1} it is sufficient to ensure the nozzle lies inside $\mathcal{W}_i$. When printing S_{i+1}', on the other hand, because S_{i+1} is already fabricated, the nozzle now needs to be confined in the wedge $\mathcal{W}_i'$ enclosed by ℓ_i' and ℓ_{i+1} (see Fig. 4). Upon completion of S_{2n+2}', what remains is $S^* = \mathcal{S} \cap \mathcal{W}_{2n+2}$, which can be printed by choosing a nozzle that can be contained in $\mathcal{W}_{2n+2}$ throughout the process of printing. □

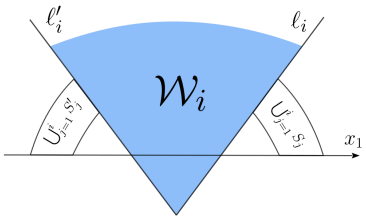

Fig. 3. Visual illustration of the collision-free region $\mathcal{W}_i$ (the blue wedge) when printing S_{i+1}.

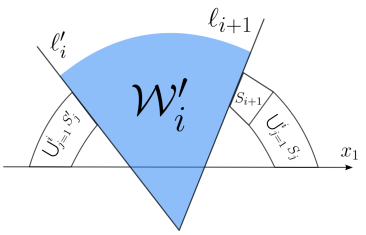

Fig. 4. Visual illustration of the collision-free region $\mathcal{W'}_i$ (the blue wedge) when printing S'_{i+1}.

Fig. 5 supplies a visual illustration of the process of printing a convex arch in a 2D workspace.

IV. Printability of a Convex Dome in a 3D Workspace

Given the results in Section III, that any convex arch is printable, one may proceed to claim that any convex dome, which is, in essence, a body of revolution generated by a convex arch, is printable.

Proposition 2. *Let $\mathcal{D} = \mathcal{D}(f_1, f_2)$ be a convex dome. Then there exists a printable partition of $\mathcal{D}$.*

Proof: Let $\mathcal{S}$ be the cross-section of $\mathcal{D}$ along the x_1x_2 plane. Follow the procedure in the proof to Proposition 1 to obtain the shapes $\{S_i\}_{i=1}^{2n+2}$ and S^*. Re-label the coordinate axes such that $\mathcal{S}$ is symmetric about the x_2 axis. Let D_i be the shape generated by revolving S_i around the x_2 axis ($i = 1, ..., 2n+2$), and D^* the body of revolution generated by S^*. It is desired to show that $\mathcal{D}$ can be printed by printing the shapes in the following order:

$$D_1 \to D_2 \to \cdots \to D_{2n+2} \to D^*. \tag{18}$$

Let $\{\ell_i\}_{i=0}^{2n+2}$ be as defined in the proof to Proposition 1 and let $\{L_i\}_{i=1}^{2n+2}$ be the surfaces generated by rotating them around the x_2-axis. Also, let $D_{i,\phi} = D_i \cap K_\phi$, where $\phi \in [0, 2\pi)$ and

$$K_\phi = \left\{ \begin{bmatrix} x_1 \\ x_2 \\ x_3 \end{bmatrix} \in \mathbb{R}^3 : \begin{bmatrix} \cos\phi \\ \sin\phi \end{bmatrix} = \frac{1}{\sqrt{x_1^2 + x_3^2}} \begin{bmatrix} x_1 \\ x_3 \end{bmatrix} \right\}. \tag{19}$$

By (5)-(7), one knows that each $D_{i,\phi}$ can be printed in a 2D space within the overhang constraints, as long as one takes the line $L_{i-1} \cap K_\phi$ as the printing bed. Now, rather than printing the 2D cross sections one by one, construct the new deposition trajectories as follows:

1) Consider the cross section $D_{i,0} = D_i \cap K_0$. Let $\{\ell_{i-1,j}\}_j$ be the deposition trajectory to print the j-th layer of $D_{i,0}$ and $L_{i-1,j}$ the surface of revolution generated by $\ell_{i-1,j}$.
2) For each point $p \in \ell_{i-1,j}$, let C_p be the circle resulted by revolving p around the x_2-axis.

And then, the j-th layer of D_i, which can be regarded as a body of revolution generated by $\ell_{i-1,j}$, can be printed by traversing the circles C_p ($p \in \ell_{i-1,j}$). One may refer to Fig. 8 for visualization of the deposition circles to be printed when fabricating $L_{i-1,j}$. By rotational symmetry of D_i, one may conclude that each D_i can be printed within the overhang constraints if, for any $\phi \in [0, 2\pi)$ when the nozzle deposits material on $D_{i,\phi}$ the printing bed is the plane tangent to L_{i-1} at $\ell_{i-1,\phi} = L_{i-1} \cap K_\phi$.

As for the collision constraints, when printing D_i, it is easy to see that one needs to ensure that the nozzle lies completely inside the cone-shaped region $\widehat{\mathcal{W}}_{i-1}$, which can be regarded as the body of revolution generated by $\mathcal{W}_{i-1}$ (which is defined in the proof to Proposition 2).

Upon completion of D_{2n+2}, what remains is to print D^*. Similar to S^*, since it is fully supported by L_{2n+2}, it can be safely printed regardless of its inclination angle w.r.t. the printing bed. As for the collision constraint, all one needs to ensure is that the nozzle is contained in $\widehat{\mathcal{W}}_{2n+2}$. □

Fig. 6 illustrates how the approach for printing 2D convex arches (in the proof in Section III) is extended to 3D, while Fig. 7 shows the relative positioning between the nozzle and the fabricated geometry. Also, as shown in Fig. 7, fabrication of each sub-region may be achieved by the coordinate motion between the fabricated part rotating and the nozzle traversing the deposition paths of the sub-region's radial cross-section.

V. Feasibility Testing

As presented in sections III and IV, AM of certain subregions that serve to close the void may require the use of a nozzle with an angle offset between the nozzle axis and the normal axis of the deposition surface. Additionally, Section IV implies the necessity of AM on a rotating printing bed, which was proven feasible by [22]. The feasibility of AM using a nozzle angle offset, on the other hand, is evaluated using an LDO Motion Voron 0.2 3D printer. Fig. 9 shows the Voron 0.2 modified to create a 45° angle between the nozzle axis and the normal axis of the printbed. The four nozzles shown in Fig. 10 are considered in this initial testing. The nozzles considered include: Fig. 10(a) a commercial nozzle adapter with 0.4mm airbrush, Fig. 10(b) a custom nozzle with a fillet tip, Fig. 10(c) a custom nozzle with a chamfer tip, and Fig. 10(d) a custom nozzle with a bevel tip. Each nozzle is evaluated qualitatively by printing the "XYZ 20mm Calibration Cube" (UltiMaker Thingiverse Thing 1278865).

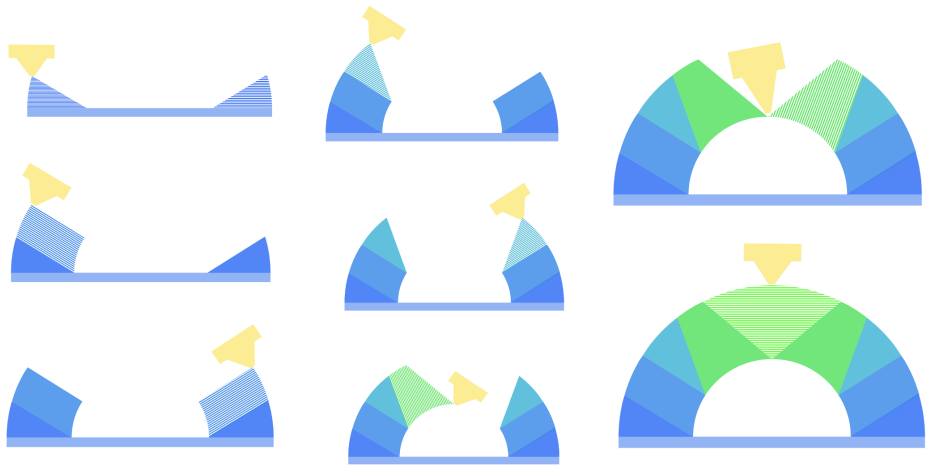

Fig. 5. Overview of the 2D printing process, which proceeds left-right in the order from top to bottom. The opaque blue strip represents the printing bed, and the parallel lines represent the deposition paths of the nozzle. As one may see in steps 6 and 7, the nozzle may not be normal to its deposition paths when closing up the void. Note also that an alternate nozzle may be necessary in step 7.

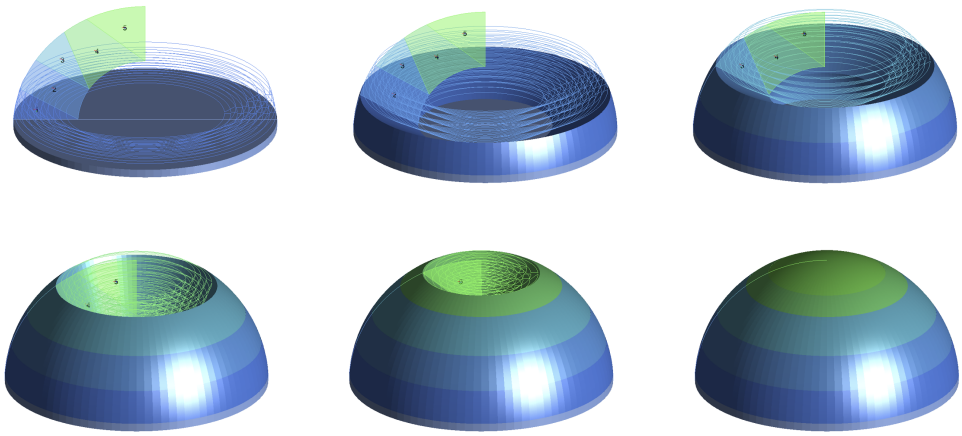

Fig. 6. A graphical explanation of how the method in Section III is extended to a 3D workspace. In this example, the target geometry is the body of revolution generated by the convex arch in Fig. 5. The printing process proceeds top-down in the order from left to right. In each subfigure, the printed part is represented as a solid geometry, whereas the curves outline the surfaces to be printed to fabricate the next subregion.

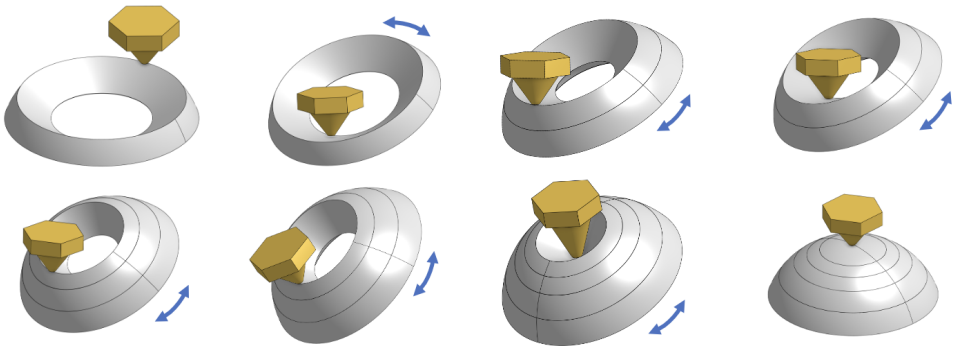

Fig. 7. Overview of the printing process, which proceeds top-down in the order from left to right. The blue arrows indicate the movement of the printed part with respect to the deposition nozzle. Similar to the 2D case, an alternate nozzle may be used when closing up the void.

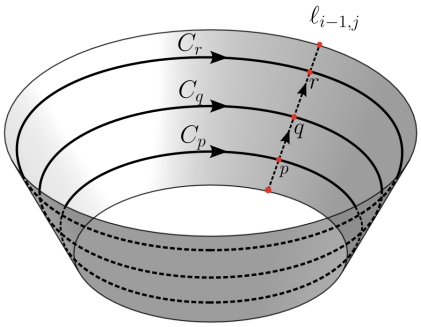

Fig. 8. Visual illustration of $\ell_{i-1,j}$ $(i = 1, ..., 2n + 2)$ and $L_{i-1,j}$, as well as the deposition trajectories to be traversed to print $L_{i-1,j}$. p, q, and r (the three red dots in the middle of $\ell_{i-1,j}$) are three distinct points on $\ell_{i-1,j}$, while C_p, C_q, and C_r are their corresponding deposition circles. The arrows on $\ell_{i-1,j}$ indicate the direction in which the deposition circles "propagate".

VI. Results

Using the modified Voron 0.2 (Fig. 9), each of the nozzles shown in Fig. 10 is used to print the "XYZ 20mm Calibration Cube." Results from each nozzle are summarized in Fig. 11. Fig. 11(a) is the best print achieved using the commercial nozzle adapter with 0.4mm airbrush shown in Fig. 10(a). Fig. 11(b) is the best print achieved using the custom nozzle with a fillet tip shown in Fig. 10(b). Fig. 11(c) is the best print achieved using the custom nozzle with a chamfer tip shown in Fig. 10(c). Fig. 11(d) is the best print achieved using the custom nozzle with a bevel tip shown in Fig. 10(d).

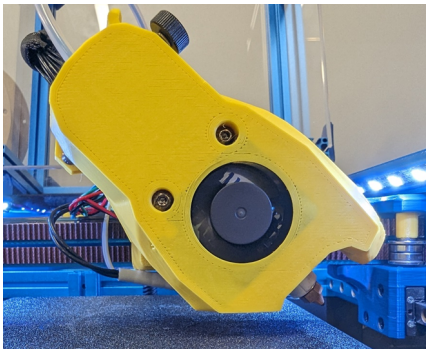

Fig. 9. Modified LDO Voron 0.2 printer to evaluate the feasibility of non-normal AM with the nozzle $45°$ to the printing bed.

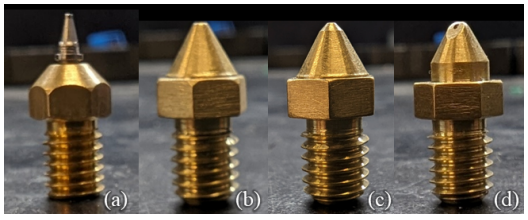

Fig. 10. Nozzles evaluated in non-normal feasibility testing.

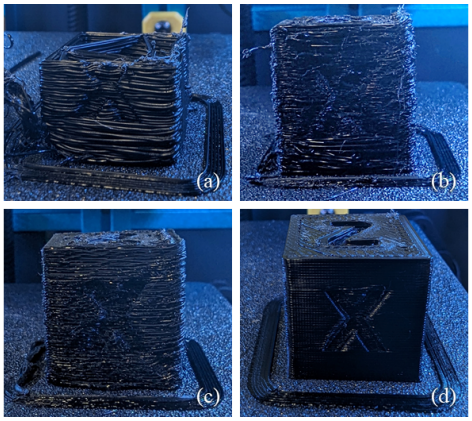

Fig. 11. Printing results for each of the four nozzle geometries used for non-normal feasibility testing. Subplot (d) highlights the superior performance of the bevel-tip nozzle design shown in Fig. 10(d).

VII. Discussion & Future Work

This work extends the capability of AM by presenting a novel method for AM of overhanging features in parts containing revolved geometries. Methods presented leverage a keystone approach presented in [21] and experimental results demonstrate successful additive fabrication using the keystone angular offset. Methods are described in the context of dome-shaped structures, and work can be extended using methods described in [16]–[18]. Under the assumption of a 3-DoF task space, this work provides a decomposition approach to achieve support-free AM for convex arch-shaped geometries. With a theoretical success in verifying its viability, this approach is smoothly migrated to the 6-DoF task space by identifying each part of the decomposed arch with a body of revolution it generates. In addition, this approach generalizes the material deposition in a FFF application such that the deposition head is no longer required to be normal to the path it traverses. To evaluate the feasibility of non-normal AM, experimental testing was conducted using a series of nozzles set to a fixed $45°$ offset angle relative to the printbed. The results presented in Fig. 11(a)-(c) suggest that deposition with an angled nozzle is infeasible using commercially available or lightly modified nozzle geometries. By introducing a beveled nozzle geometry, Fig. 11(d) demonstrates feasibility when printing with an angled nozzle. These results, when combined with existing work leveraging robotic AM with a rotating build plate (e.g. [22]), suggest generation of a physical part using the methods described in Section IV is feasible. Near-term extensions to this work will include additional experimental testing for fabrication of a closed void, decomposition of dome-shaped geometries without rotational symmetry, as well as part geometries consisting of multiple dome structures (e.g. a 3D array of closed voids that altogether constitute an architected material sample), as well as automation of the decomposition process as an algorithm (e.g., given a model, generating its printable partition by numerically solving an optimization problem).

REFERENCES

[1] M.-S. Pham, C. Liu, I. Todd, and J. Lertthanasarn, "Damage-tolerant architected materials inspired by crystal microstructure," *Nature*, vol. 565, no. 7739, pp. 305–311, 2019.

[2] J. R. Greer and V. S. Deshpande, "Three-dimensional architected materials and structures: Design, fabrication, and mechanical behavior," *MRS Bulletin*, vol. 44, no. 10, pp. 750–757, 2019.

[3] Z. Zhang, H. Lei, H. Yang, M. Chen, C. Wang, H. Yang, and D. Fang, "Novel multifunctional lattice composite structures with superior load-bearing capacities and radar absorption characteristics," *Composites Science and Technology*, vol. 216, p. 109064, 2021.

[4] G. Dreifus, K. Goodrick, S. Giles, M. Patel, R. M. Foster, C. Williams, J. Lindahl, B. Post, A. Roschli, L. Love *et al.*, *Additive manufacturing technologies: 3D printing, rapid prototyping, and direct digital manufacturing*, I. Gibson, D. Rosen, and B. Stucker, Eds. Johnson Matthey, 2015, no. 3.

[5] A. T. Gaynor, N. A. Meisel, C. B. Williams, and J. K. Guest, "Topology optimization for additive manufacturing: considering maximum overhang constraint," in *15th AIAA/ISSMO multidisciplinary analysis and optimization conference*, 2014, p. 2036.

[6] T. E. Johnson and A. T. Gaynor, "Three-dimensional projection-based topology optimization for prescribed-angle self-supporting additively manufactured structures," *Additive Manufacturing*, vol. 24, pp. 667–686, 2018.

[7] A. Clausen, N. Aage, and O. Sigmund, "Exploiting additive manufacturing infill in topology optimization for improved buckling load," *Engineering*, vol. 2, no. 2, pp. 250–257, 2016.

[8] J. Wu, C. C. Wang, X. Zhang, and R. Westermann, "Self-supporting rhombic infill structures for additive manufacturing," *Computer-Aided Design*, vol. 80, pp. 32–42, 2016.

[9] G. Dreifus, K. Goodrick, S. Giles, M. Patel, R. M. Foster, C. Williams, J. Lindahl, B. Post, A. Roschli, L. Love *et al.*, "Path optimization along lattices in additive manufacturing using the chinese postman problem," *3D Printing and Additive Manufacturing*, vol. 4, no. 2, pp. 98–104, 2017.

[10] P. Gupta, B. Krishnamoorthy, and G. Dreifus, "Continuous toolpath planning in a graphical framework for sparse infill additive manufacturing," *Computer-Aided Design*, vol. 127, p. 102880, 2020.

[11] L. Wang, K. Saito, Y. Gotou, and Y. Okabe, "Design and fabrication of aluminum honeycomb structures based on origami technology," *Journal of Sandwich Structures & Materials*, vol. 21, no. 4, pp. 1224–1242, 2019.

[12] J. Clark, K. Hurysz, K. Lee, J. Cochran, and T. Sanders Jr, "Stainless steel hollow sphere foams-fabrication, carburization, and properties," GEORGIA INST OF TECH ATLANTA SCHOOL OFMATERIALS SCIENCE AND ENGINEERING, Tech. Rep., 1998.

[13] P. M. Bhatt, R. K. Malhan, A. V. Shembekar, Y. J. Yoon, and S. K. Gupta, "Expanding capabilities of additive manufacturing through use of robotics technologies: A survey," *Additive manufacturing*, vol. 31, p. 100933, 2020.

[14] P. M. Bhatt, R. K. Malhan, P. Rajendran, and S. K. Gupta, "Building free-form thin shell parts using supportless extrusion-based additive manufacturing," *Additive Manufacturing*, vol. 32, p. 101003, 2020.

[15] Y. J. Yoon, M. Yon, S. E. Jung, and S. K. Gupta, "Development of three-nozzle extrusion system for conformal multi-resolution 3d printing with a robotic manipulator," in *International Design Engineering Technical Conferences and Computers and Information in Engineering Conference*, vol. 59179. American Society of Mechanical Engineers, 2019, p. V001T02A024.

[16] C. Wu, C. Dai, G. Fang, Y.-J. Liu, and C. C. Wang, "Robofdm: A robotic system for support-free fabrication using fdm," in *2017 IEEE International Conference on Robotics and Automation (ICRA)*. IEEE, 2017, pp. 1175–1180.

[17] Y. Murtezaoglu, D. Plakhotnik, M. Stautner, T. Vaneker, and F. J. van Houten, "Geometry-based process planning for multi-axis support-free additive manufacturing," *Procedia CIRP*, vol. 78, pp. 73–78, 2018.

[18] X. Xiao and S. Joshi, "Process planning for five-axis support free additive manufacturing," *Additive Manufacturing*, vol. 36, p. 101569, 2020.

[19] P. M. Bhatt, A. Kulkarni, R. K. Malhan, B. C. Shah, Y. J. Yoon, and S. K. Gupta, "Automated planning for robotic multi-resolution additive manufacturing," *Journal of Computing and Information Science in Engineering*, vol. 22, no. 2, 2022.

[20] L. Yuan, Z. Pan, J. Polden, D. Ding, S. van Duin, and H. Li, "Integration of a multi-directional wire arc additive manufacturing system with an automated process planning algorithm," *Journal of Industrial Information Integration*, vol. 26, p. 100265, 2022.

[21] J. Liu, M. Armand, and M. D. M. Kutzer, "Toward additive manufacturing of architected materials: A planar analysis," in *ASME International Mechanical Engineering Congress and Exposition (IMECE)*, vol. 3, 2023, p. V003T03A005. [Online]. Available: https://doi.org/10.1115/IMECE2023-113456

[22] Y. Ding, R. Dwivedi, and R. Kovacevic, "Process planning for 8-axis robotized laser-based direct metal deposition system: a case on building revolved part," *Robotics and Computer-Integrated Manufacturing*, vol. 44, pp. 67–76, 2017.